

Direct sulfuric acid formation from the gas-phase oxidation of reduced-sulfur compounds

Received: 3 March 2023

Accepted: 1 August 2023

Published online: 10 August 2023

Check for updates

Torsten Berndt¹✉, Erik H. Hoffmann¹, Andreas Tilgner¹,
Frank Stratmann² & Hartmut Herrmann¹

Sulfuric acid represents a fundamental precursor for new nanometre-sized atmospheric aerosol particles. These particles, after subsequent growth, may influence Earth's radiative forcing directly, or indirectly through affecting the microphysical and radiative properties of clouds. Currently considered formation routes yielding sulfuric acid in the atmosphere are the gas-phase oxidation of SO₂ initiated by OH radicals and by Criegee intermediates, the latter being of little relevance. Here we report the observation of immediate sulfuric acid production from the OH reaction of emitted organic reduced-sulfur compounds, which was speculated about in the literature for decades. Key intermediates are the methylsulfonyl radical, CH₃SO₂, and, even more interestingly, its corresponding peroxy compound, CH₃SO₂OO. Results of modelling for pristine marine conditions show that oxidation of reduced-sulfur compounds could be responsible for up to ~50% of formed gas-phase sulfuric acid in these areas. Our findings provide a more complete understanding of the atmospheric reduced-sulfur oxidation.

Since more than 3 decades, reduced organic sulfur compounds have been recognized as substantial biogenic emissions contributing to Earth's sulfur cycle. The sulfur cycle is highly relevant for the Earth's climate due to the ability of the sulfur compound's oxidation products, sulfuric acid (H₂SO₄) and methane sulfonic acid (MSA, CH₃SO₃H), to generate new airborne particles that effectively scatter incoming solar radiation and affect the formation of cloud condensation nuclei (CCN)^{1,2}. CCN in turn may have significant influences on the microphysical and radiative properties³ and lifetime⁴ of clouds.

Globally, the most important organic sulfur compound is dimethyl sulfide (DMS, CH₃SCH₃) with an annual emission rate of ~30 million metric tons of sulfur, followed by methylthiol (MeSH, CH₃SH) and, to a lesser extent, dimethyl disulfide (DMDS, CH₃SSCH₃)⁵. A large number of experimental and theoretical studies have been conducted to ascertain their atmospheric degradation pathways, especially for DMS^{6–18}, representing the data base for atmospheric

models^{19–22}. The reaction scheme in Fig. 1 summarises the current knowledge on product formation starting from the methylthiyl (CH₃S) and methylsulfonyl radical (CH₃SO₂), both formed as important intermediates in the gas-phase oxidation of CH₃SH, DMS and DMDS. To the best of our knowledge, up to now there is no experimental evidence for the direct gas-phase formation of H₂SO₄, other than via SO₂ oxidation by OH radicals^{23,24} or Criegee intermediates^{25,26}, although this has been speculated about in the literature for long^{27,28} and such pathways have already been implemented in models^{19–22}.

Here we experimentally demonstrate the direct formation of H₂SO₄ from the OH radical-initiated gas-phase oxidation of organic sulfur compounds by its direct mass spectrometric detection in two flow systems^{29–31} under atmospheric conditions with residence times of 7.9 and 32 s. Accompanied modelling shows the importance of this direct pathway for the total H₂SO₄ formation in the atmosphere.

¹Atmospheric Chemistry Department (ACD), Leibniz Institute for Tropospheric Research (TROPOS), 04318 Leipzig, Germany. ²Atmospheric Microphysics Department (AMP), Leibniz Institute for Tropospheric Research (TROPOS), 04318 Leipzig, Germany. ✉e-mail: berndt@tropos.de

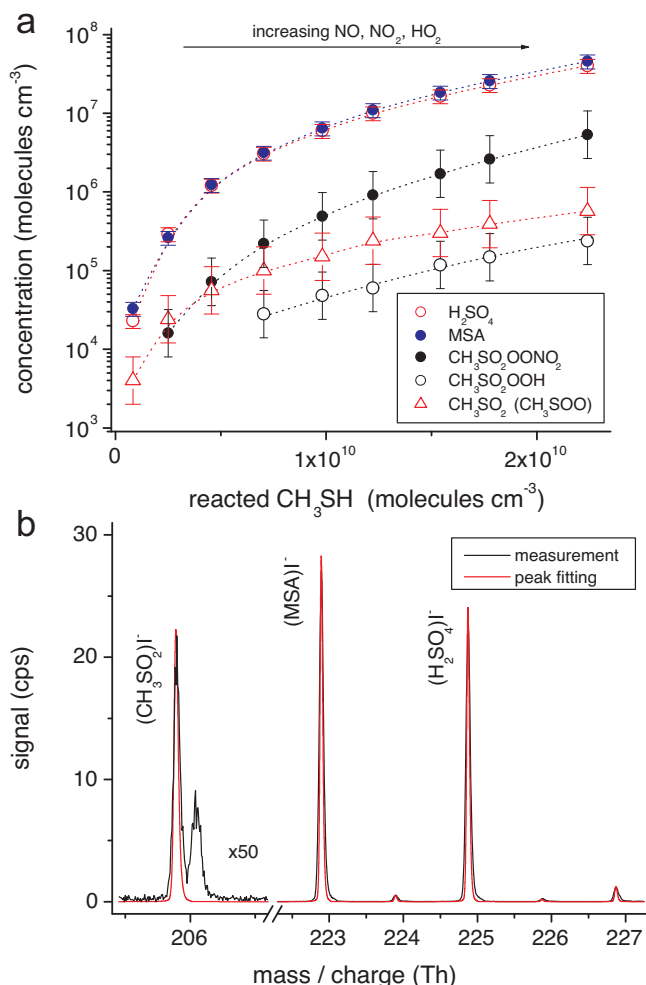


Fig. 2 | Product detection from CH₃S oxidation using ionisation by iodide. Experiments on OH + CH₃SH for CH₃S production have been conducted in the free-jet flow system, $t = 7.9$ s, at r.h. = 10%. OH radicals were produced from IPN (isopropyl nitrite) photolysis, i.e. OH radical generation via $\text{NO} + \text{HO}_2 \rightarrow \text{NO}_2 + \text{OH}$. Increasing OH radical levels for rising CH₃SH conversion were linked by increasing concentrations of NO, NO₂ and HO₂ due to increasing IPN conversion in the photolysis. Reactant concentrations are stated in Supplementary Table 1. Source data are provided as a Source Data file. **a** Detected products are given as a function of converted CH₃SH. Data for H₂SO₄ and MSA (methane sulfonic acid) are based on absolute calibration with an uncertainty of ~20%. Other concentrations represent lower limits with an uncertainty of a factor of 2. **b** Measured raw spectrum from 10 min data accumulation compared with calculated signals of iodide adducts with CH₃SO₂, H₂SO₄ and MSA from peak fitting.

the presence of sufficiently high CH₃SH or other substances serving as H-atom donor. A similar behaviour of the H₂SO₄/MSA ratio was also observed in OH + DMDS experiments varying the DMDS concentrations (Supplementary Fig. 4). Here, almost exclusive H₂SO₄ formation can be expected for DMDS concentrations below 10¹⁰ molecules cm⁻³.

Because atmospheric CH₃SH and DMDS concentrations are clearly smaller than 10¹⁰ molecules cm⁻³ (400 ppt), see attached Supplementary Dataset 1 and ref. 5, CH₃SO₃ decomposition (pathway 17) forming finally the direct H₂SO₄ most likely dominates the fate of CH₃SO₃ for atmospheric conditions (Fig. 3 and Supplementary Fig. 4). MSA formation according to CH₃SO₃ + RH for RH ≡ CH₃SH or DMDS (pathway 19) has to be of minor importance. It is speculative whether or not other hydrocarbons RH in the atmosphere could efficiently form MSA via pathway 19.

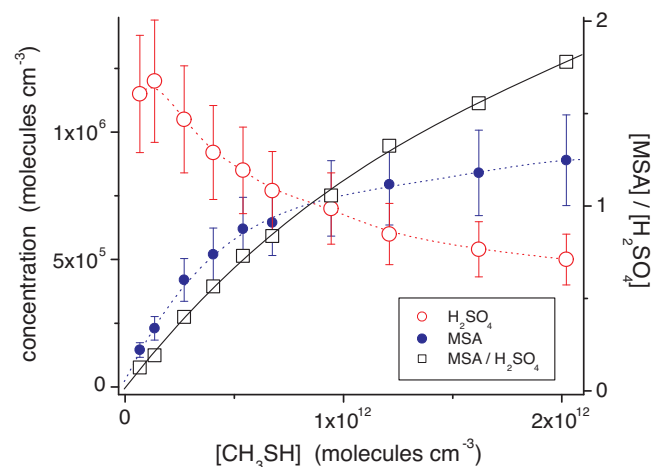


Fig. 3 | Concentrations of H₂SO₄ and MSA (methane sulfonic acid), and the MSA/H₂SO₄ ratio as a function of CH₃SH concentration. Experiments on OH + CH₃SH were carried out in the free-jet flow system at r.h. = 10% and a reaction time of 7.9 s using IPN (isopropyl nitrite) photolysis for OH radical generation. Reactant concentrations are stated in Supplementary Table 1. The error bars for H₂SO₄ and MSA depict the uncertainty of ~20% based on the uncertainty in the calibration factor. Source data are provided as a Source Data file.

Formation routes to direct H₂SO₄

We evaluated the impact of atmospheric trace gases, i.e. ozone, RO₂ radicals, NO and NO₂, in the process of direct gas-phase H₂SO₄ formation with separate experiments starting from the OH radical reactions with CH₃SH and DMDS (Fig. 4). While OH + CH₃SH represents a clean source of CH₃S with a reported formation yield of 1.1 ± 0.2 ³⁴, OH + DMDS is expected to form CH₃S and CH₃SOH^{39,40}, which further reacts with ozone leading mainly to CH₃SO₂ with a yield close to unity for high enough ozone concentrations³². The OH + DMS reaction was not considered in these experiments because of its complexity^{9,11}, which complicates the investigation of selected pathways. Reaction conditions were chosen in such a way that intermediate concentrations were kept as low as possible in order to suppress unwanted bimolecular steps not relevant in the atmosphere. For this reason, the amount of reacted CH₃SH and DMDS was limited to a few 10⁸ molecules cm⁻³. Gas-phase H₂SO₄ formation starting from the reaction of SO₂ with OH radicals or Criegee intermediates was again small in these measurement series and did not influence the results of direct H₂SO₄ formation significantly, see also Methods.

Ozone: No significant H₂SO₄ formation from OH + CH₃SH was observed for ozone concentrations of up to 2×10^{12} molecules cm⁻³ (~80 ppb) in the free-jet flow system with the short reaction time of 7.9 s. H₂SO₄ became detectable in the laminar flow tube (LFT) with a reaction time of 32 s indicating a relatively slow process of direct H₂SO₄ formation (Fig. 4a). Big differences in the H₂SO₄ yields of more than an order of magnitude were measured using either OH + CH₃SH for CH₃S generation or OH + DMDS forming CH₃S and most likely CH₃SO₂ with high yields. Considering CH₃SO₂ as the needed intermediate for direct H₂SO₄ formation (Fig. 1), CH₃S's oxidation obviously proceeds only with a small share via CH₃SO₂, e.g. $\leq 9\%$ for an ozone concentration of 5.7×10^{11} molecules cm⁻³ (Fig. 4a) taking OH + DMDS with a CH₃SO₂ yield of unity as the reference. Moreover, OH + CH₃SH experiments with heavy ozone (¹⁸O₃) revealed the absence of H₂SO₄ containing three ¹⁸O atoms (Supplementary Fig. 5) as expected from the reaction sequence 3, 6b and 9 (Fig. 1). We largely measured H₂SO₄ with one ¹⁸O atom consistent with the reaction sequence 1/-1, 2 and 9. The findings imply the dominance of pathway 6a over 6b or in fact the irrelevance of pathway 6b, allowing for the importance of ozone reactions in the CH₃S oxidation^{8,34,41}. This can be

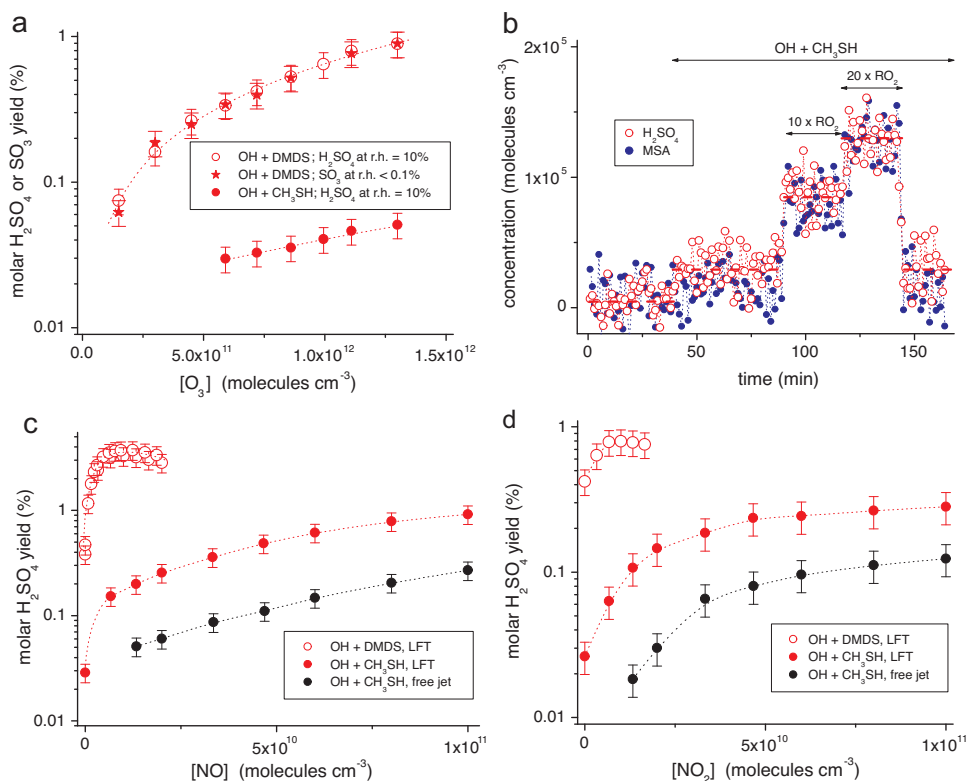


Fig. 4 | Impact of trace gases on direct H₂SO₄ formation using ionisation by nitrate. Experiments were conducted either in the free-jet flow system, $t = 7.9$ s, or in the laminar flow tube (LFT), $t = 32$ s, at r.h. = 10% (or <0.1%) using tetramethyl ethylene (TME) ozonolysis for OH radical production. Reactant concentrations are given in Supplementary Table 1. Error bars represent the uncertainty of ~20% in the absolute calibration. Source data are provided as a Source Data file. **a** Formation of H₂SO₄ and SO₃ as a function of ozone measured in the LFT. Reacted CH₃SH was in the range $(7.6\text{--}17) \times 10^7$ and $(2.1\text{--}18) \times 10^7$ molecules cm⁻³ for DMDS (dimethyl

disulfide). **b** H₂SO₄ and MSA (methane sulfonic acid) formation from OH + CH₃SH depending on RO₂ radical concentrations, CH₃C(O)CH₂O₂ and CH₃O₂, in the LFT. Rising RO₂ levels were achieved by stepwise increase of TME and corresponding CH₄ additions keeping reacted CH₃SH constant at $\sim 7.6 \times 10^7$ molecules cm⁻³. Highest CH₃C(O)CH₂O₂ and CH₃O₂ concentrations were 1.0×10^9 and 8.8×10^8 molecules cm⁻³, respectively, calculated from an extended model (Supplementary Table 4). **c** H₂SO₄ formation yields as a function of NO addition. **d** H₂SO₄ formation yields as a function of NO₂ addition.

explained by the high exothermicity of the CH₃SO + O₃ reaction forming the chemically excited CH₃SO₂* that rapidly decomposes to SO₂ and CH₃ before it is thermalised⁴².

The small H₂SO₄ yields < 1% for atmospheric ozone concentrations, even under conditions of the preferred CH₃SO₂ generation from OH + DMDS, support the efficient decomposition of CH₃SO₂ (pathway 8), which is in line with the high SO₂ yields reported recently^{32,33}. SO₃ yields measured under dry conditions, r.h. < 0.1%, were in very good agreement with the H₂SO₄ yields at r.h. = 10% (Fig. 4a) confirming SO₃ as the precursor of H₂SO₄ (pathways 17 and 18 in Fig. 1).

An ozone concentration of 5.7×10^{11} molecules cm⁻³ (~23 ppb) was chosen in the following experiments, which stands for an average concentration over pristine oceans⁴³, making our findings applicable to the atmospheric reaction system.

RO₂ radicals: We detected a distinct impact of RO₂ radicals on the formation of H₂SO₄ and MSA (Fig. 4b). Main RO₂ radicals in the reaction system are CH₃C(O)CH₂O₂, formed in the course of OH radical generation via TME ozonolysis^{44,45}, and CH₃O₂ as the by-product of SO₂ in the oxidation of CH₃SH and DMDS^{32,33} as well as from OH + CH₄ in the case of CH₄ additions. In the OH + CH₃SH reaction, we increased in a two-step process the concentrations of CH₃C(O)CH₂O₂ and CH₃O₂ radicals, first by a factor of ~10, i.e. from 6.2×10^7 to 5.7×10^8 and from 4.0×10^7 to 4.4×10^8 molecules cm⁻³, respectively, leading to enhanced H₂SO₄ formation by a factor of ~3.5 for constant CH₃SH conversion (Fig. 4b). Further doubling of the RO₂ concentrations led to further rise in H₂SO₄ productions. The MSA formation, however, increased stronger than that of H₂SO₄, which became more visible from a similar experiment on OH + DMDS (Supplementary Fig. 6). Furthermore, we

observed predominate MSA formation in a reaction system with HO-C₆H₁₂O₂ along with CH₃C(O)CH₂O₂ as the main RO₂ radicals (Supplementary Fig. 7). It can be speculated that most likely CH₃SO₂OO reacted with RO₂ radicals either via the alkoxy channel (pathway 15 in Fig. 1), forming finally H₂SO₄, or via the dismutation channel (pathway 16 in Fig. 1), similar to the well-known chemistry of carbon-centred RO₂ radicals⁴⁶, leading to MSA. The branching ratio of pathways 15 vs. 16 appears to be dependent on the structure of the reacting RO₂ radical. Other RO₂ driven pathways, influencing the product formation, cannot be ruled out.

Nitrogen oxide (NO): Addition of NO substantially accelerated the H₂SO₄ formation in all experiments (Fig. 4c) supporting the potential importance of CH₃SO₂OO for H₂SO₄ formation, here via pathway 14 (Fig. 1). An increase in the H₂SO₄ production by a factor of ~4 (Supplementary Fig. 8) was measured using a NO concentration of 1×10^9 molecules cm⁻³ similar to the behaviour observed for elevated RO₂ concentrations (Fig. 4b and Supplementary Fig. 6). This indicates rate coefficients k_{14} and k_{15} for the reaction of CH₃SO₂OO with NO and RO₂, respectively, being in the same range. Comparison of results for relatively low NO concentrations of < 10^{10} molecules cm⁻³ in the LFT showed more than one order of magnitude higher H₂SO₄ yields from the oxidation of DMDS relative to CH₃SH, in line with the findings from the pure ozone-driven reaction (Fig. 4a). For elevated NO levels, other NO reactions presumably disturbed the CH₃SO₂ formation from OH + DMDS and inhibited further rise of the H₂SO₄ yield. Further NO reactions in the CH₃S oxidation could also negatively impact the H₂SO₄ formation, such as CH₃S + NO → CH₃SNO¹⁰ or CH₃SOO + NO → CH₃SO + NO₂¹⁰ (pathway 5) resulting finally in SO₂ formation via

pathway 6a (Fig. 1). The higher H₂SO₄ yields from OH + CH₃SH measured in the LFT at t = 32 s point again to a slow process of H₂SO₄ formation that is far away from completeness for the reaction time of 7.9 s in the free-jet flow system.

Nitrogen dioxide (NO₂): Addition of NO₂ featured a similar effect for the rise of H₂SO₄ yields (Fig. 4d) as observed for NO (Fig. 4c), albeit the NO₂ impact was less pronounced. It is supposed in the literature that NO₂ reacts with CH₃SO₂ forming CH₃SO₃ (pathway 10) which finally leads to H₂SO₄ analogous to the ozone-mediated route (pathway 9)⁹. This set of experiments confirmed again the much higher potential of H₂SO₄ formation starting from OH + DMDS regarding OH + CH₃SH, as well as the slow formation rate of the direct H₂SO₄ production. H₂SO₄ production almost doubled as the result of a NO₂ addition of 6.7×10^9 molecules cm⁻³ in the LFT experiments (Fig. 4d), indicating nearly the same reaction rate in the reaction of CH₃SO₂ with ozone and NO₂ (pathways 9 and 10 in Fig. 1), [O₃] = 5.7×10^{11} molecules cm⁻³. This leads to $k_9/k_{10} \sim 1/85$ being in good agreement with the rate coefficient ratio currently used in models^{21,22}. The experiments with NO₂ addition did not allow any conclusions regarding the relative importance of the product channels 7a and 7b from CH₃SO + NO₂.

In summary, the experiments provided evidence for the promoting effect of each of the four important trace gases for the direct H₂SO₄ formation. The relatively strong impact caused by RO₂ radicals and NO (Fig. 4b and 4c) was surprising, which further highlights CH₃SO₂OO radicals as important intermediates.

Application to the atmosphere

Adjustments in the H₂SO₄ yields were needed in order to apply the laboratory findings for atmospheric conditions. The incompleteness of the CH₃SO₃ conversion due to the short reaction times led to a correcting factor of 1.6 for the H₂SO₄ yields in the LFT using $k_{17} = 0.076$ s⁻¹ at 295 ± 2 K, see Methods. Relatively high CH₃SH and DMDS concentrations in the experiments, not present in the atmosphere, necessitated further adjustment by a factor of ~1.5 to allow for the suppression of H₂SO₄ formation in their competing reaction with CH₃SO₃ forming MSA (pathway 19 in Fig. 1), see Fig. 3 and Supplementary Fig. 4. Adjusted H₂SO₄ yields for low-NO_x conditions and [O₃] = 5.7×10^{11} molecules cm⁻³ were estimated to be $0.074 \pm 0.015\%$ per formed CH₃S and $0.82 \pm 0.02\%$ per formed CH₃SO₂ (Fig. 4a) assuming a CH₃SO₂ yield of unity from OH + DMDS. The yields increased to $0.11 \pm 0.02\%$ (CH₃S) and $1.2 \pm 0.2\%$ (CH₃SO₂) incorporating the “RO₂ effect” (Fig. 4b) for total RO₂ radical concentrations of $\sim 3 \times 10^8$ molecules cm⁻³, that represents an average RO₂ level during main CH₃S and CH₃SO₂ production at noon (Supplementary Fig. 9). The ratio $k_8/(k_9 \times [O_3]) \sim 120$ ($k_8/k_9 \sim 7 \times 10^{13}$ molecules cm⁻³) followed from the ozone-driven experiments on OH + DMDS with a H₂SO₄ yield of 0.82%, that strongly favours SO₂ formation from CH₃SO₂ (pathway 8) being consistent with the high SO₂ yields measured^{32,33}. This k_8/k_9 ratio, however, is in contrast to the implementation in latest atmospheric models, $k_8/k_9 = 9.5 \times 10^{11}$ molecules cm⁻³^{21,22}, leading to severe overestimation of the modelled CH₃SO₃ production.

Atmospheric impact

Process model simulations were performed with a complex multi-phase chemistry mechanism MCM/CAPRAM^{47,48} for six different scenarios (Methods and Supplementary Table 2) to assess the importance of the direct gas-phase formation pathway of H₂SO₄ from DMS and CH₃SH oxidation relative to the OH + SO₂ reaction under pristine marine conditions. Oxidation of DMDS was neglected because of its relatively small emission⁵. The model is able to simulate typical DMS and SO₂ mixing ratios (see Supplementary Figs. 10 and 11) as measured under marine conditions (Fig. 5a and attached Supplementary Dataset 1) independent of NO_x levels assumed in the simulations (Supplementary Fig. 12). The modelled CH₃S and CH₃SO₂ formation rates are provided in Supplementary Table 3 for all six

simulations. It can be seen that NO_x can likely affect the CH₃S formation, but it is less important for CH₃SO₂ formation. The strongest impact on CH₃SO₂ production has the H_A applied. The modelled CH₃S and CH₃SO₂ formation rates together with the experimental H₂SO₄ yields of 0.11% (CH₃S), 1.2% (CH₃SO₂) and 100% (SO₂) were used to calculate the gas-phase H₂SO₄ formation rates from the different oxidation pathways and their relative contributions (Fig. 5b). For more clarity, the simulations with higher NO_x are not depicted, because of the modelled low effect on CH₃S and CH₃SO₂ formation rates in comparison with the simulation using the smaller NO emission. The data in Supplementary Table 3 reveal that the modelled CH₃S and CH₃SO₂ formation rates are only weakly affected by ten times higher NO_x emissions, whereas the considered uptake parameters are the most important influencing factors. As the result, the direct gas-phase formation of H₂SO₄ arises mainly from the DMS addition channel and can contribute up to ~50% to the overall gas-phase H₂SO₄ production. This emphasises the importance of the direct gas-phase formation route for marine conditions. Fully neglecting the share from the DMS addition channel because of inconsistent CH₃SO₂ yields currently in the literature^{9,19,49}, still a fraction of up to ~12% remains (Fig. 5b). It should be noted, that total direct gas-phase H₂SO₄ formation rates exclusively simulated by the model (Supplementary Fig. 13) exceeded those from the combined experiment/model approach (Fig. 5b) by about two orders of magnitude. A main reason for that is the inappropriate description of CH₃SO₂'s fate in the latest models^{21,22}.

The simulations indicate that the concentration ratio of SO₂ relative to the reduced-sulfur compounds, mainly DMS, is a critical parameter for the importance of the direct gas-phase H₂SO₄ formation. This becomes apparent using data from a field campaign at Baring Head, New Zealand⁵⁰, with an air mass change from anthropogenically influenced, SO₂/DMS > 10, to the clean pristine ocean regime, SO₂/DMS < 0.1 (Fig. 5c). Significant relevance of the direct gas-phase H₂SO₄ route only exists for SO₂/DMS ≤ 0.3. Thus, the direct gas-phase route could be important especially in the Southern Hemisphere, due to low SO₂/DMS ratios existing there (Fig. 5a), and in the outflow of convective marine clouds where SO₂ is reduced by scavenging and cloud chemistry.

Field studies often indicated new particle formation in the direct vicinity above marine clouds^{51,52} most likely connected to the high OH radical⁵³ and H₂SO₄ concentrations⁵⁴ observed at such locations. Updrafts of clouds can inject DMS into the free troposphere. There, we suggest that the direct gas-phase H₂SO₄ formation DMS → H₂SO₄, as identified in the present study, play an important role for gas-phase H₂SO₄ production in cloud outflows, because of the expected low SO₂/DMS ratio immediately after cloud passage and the slow overall process DMS → SO₂ → H₂SO₄. This implies that directly formed gas-phase H₂SO₄ from DMS oxidation is likely substantial for the observed new particle formation in cloud outflows, thereby affecting or even controlling the amounts of CCN available^{51,52,55}. Therefore, this study provides the impetus for further developments to incorporate and study such processes in regional and global atmospheric chemistry transport as well as climate models.

In conclusion, we experimentally demonstrated the direct formation of H₂SO₄ in the course of atmospheric gas-phase oxidation of reduced-sulfur compounds. We found strong indications for the reactions CH₃SO₂ + O₃ (pathway 9) and CH₃SO₂OO + RO₂ (pathway 15) being the rate limiting steps for H₂SO₄ production under low-NO_x conditions. The strong increase of H₂SO₄ production in the presence of NO emphasises the role of CH₃SO₂OO radicals in this reaction system. Our findings do not support considerable MSA formation via the CH₃SO₃ + HO₂ pathway.

Although the direct H₂SO₄ formation yields appear to be pretty small, for concentration ratios SO₂/DMS ≤ 0.3, i.e. for conditions as encountered especially over the oceans in the Southern

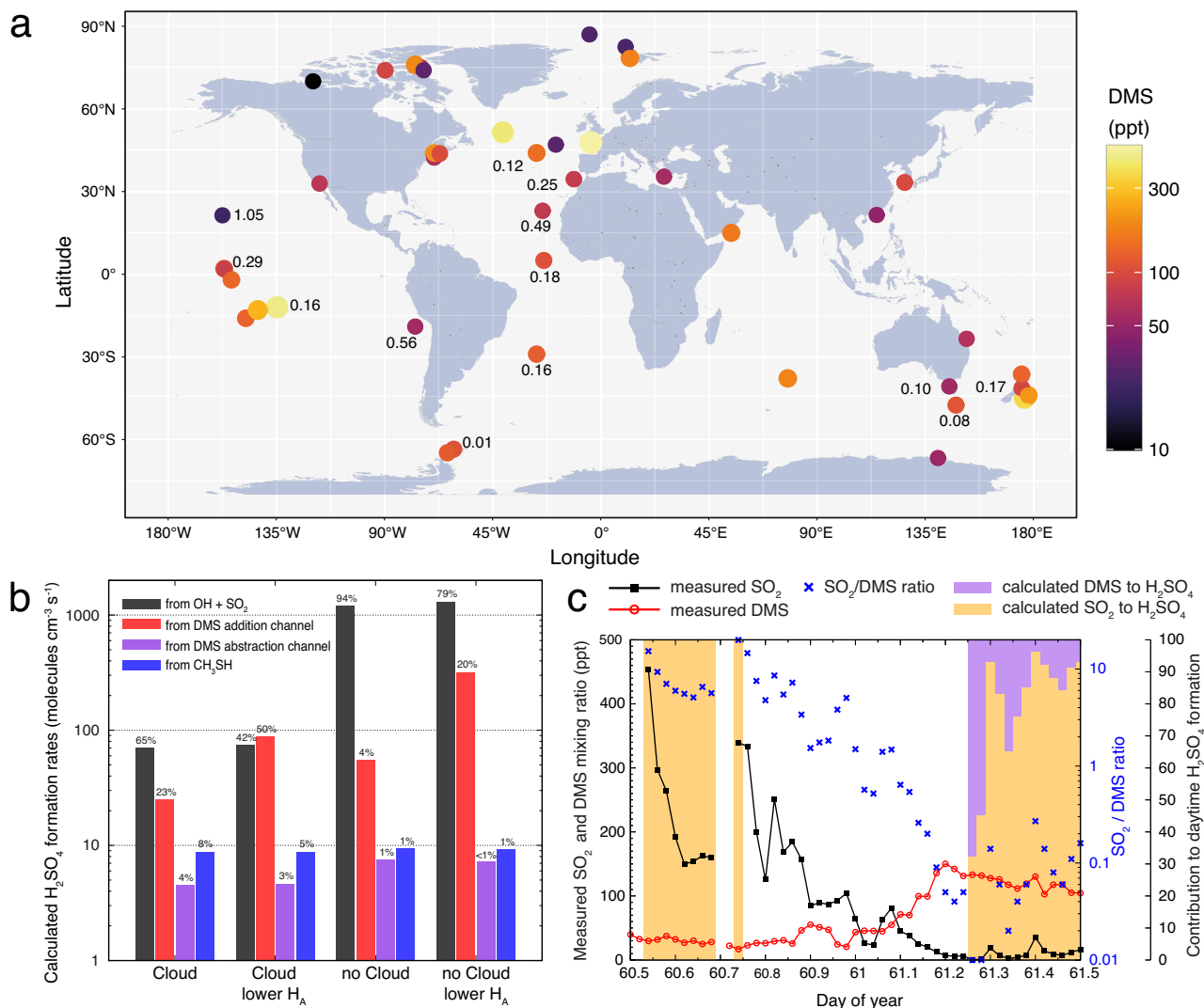


Fig. 5 | Measured DMS (dimethyl sulfide) and SO₂ data and the contribution of different pathways to H₂SO₄ formation. Source data are provided as a Source Data file. **a** Measured average DMS concentrations (colour coded) worldwide with corresponding SO₂/DMS ratios (numbers), if available. The map plot was created with R⁶⁸ using the ggplot2 package (map_data("world")). **b** Calculated H₂SO₄ formation rates from different pathways combining the modelled CH₃S and CH₃SO₂ formation rates with experimentally determined H₂SO₄ yields. The "Cloud" scenario represents simulations with cloud passages leading to lower SO₂

concentrations due to its uptake and oxidation in clouds. The simulations with "lower H_A" represent model runs using lower Henry constants H_A of DMS oxidation products (see Supplementary Table 1). **c** Reproduction of measured SO₂ (black line with squares) and DMS (red line with dots) concentrations as well as its SO₂/DMS ratio (blue crosses) from observations at Baring Head, New Zealand⁵⁰. Purple and yellow bars illustrate the calculated relative contributions of DMS (direct route) and SO₂ oxidation to total H₂SO₄ formation at daytime. The contributions are calculated based on results from "no Cloud" simulation.

Hemisphere, and/or in the outflows of clouds, the direct route could be competitive with the established OH + SO₂ path of H₂SO₄ generation.

All in all, we herewith suggest direct gas-phase formation of H₂SO₄ from reduced-sulfur compounds, such as DMS, to be an atmospherically relevant process for the production of H₂SO₄, and consequently for the formation of new particles, under, e.g. the pristine marine conditions in the Southern Hemisphere.

Methods

Experimental setup

The investigations were carried out in two flow systems, i.e. in the free-jet flow system^{30,31} and the laminar flow tube (LFT)²⁹ at 1 bar of air and a temperature of 295 ± 2 K. The flow tubes worked with different residence times, 7.9 and 32 s, respectively, that allowed to draw a conclusion regarding the rate of relatively slow processes, here on the thermal decomposition of CH₃SO₃.

The free-jet flow system consists of an outer tube (length: 200 cm, inner diameter: 16 cm) and a moveable inner tube (outer diameter: 9.5 mm) connected with a nozzle of 3 mm inner diameter. The first reactant (isopropyl nitrite (IPN) or ozone) premixed with air (5 litre min⁻¹, STP) was injected through the inner tube into the main gas stream (95 litre min⁻¹, STP), which contained the second reactant (CH₃SH and/or tetramethyl ethylene (TME) along with additions if needed) diluted in air. Downstream the nozzle, large differences of the gas velocities at the nozzle outflow (nozzle: 15.9 m s⁻¹; main flow: 0.13 m s⁻¹) and the nozzle geometry ensured rapid turbulent reactant mixing⁵⁶. The reaction time was 7.9 s, experimentally obtained by a "chemical clock". This set-up allows to carry out investigations under atmospheric conditions in absence of wall effects. IPN photolysis⁵⁷ for continuous OH radical generation in the flow system was conducted downstream the mixing point of the reactants by means of 8 NARVA 36 W Blacklight Blue lamps emitting in the range 350–400 nm. The photolysis of IPN produces NO and i-C₃H₇O radicals, which rapidly

formed acetone and HO₂ radicals in the reaction with O₂. OH radical generation finally took place via HO₂ + NO → OH + NO₂. Ozonolysis of TME⁴⁴ served as non-photolytic OH radical source under low-NO_x conditions.

The laminar flow tube (LFT) (i.d. 8 cm; total length 425 cm) consists of a first section (56 cm) containing the gas inlet system, a second middle section (344 cm) representing the reaction zone and an end section (25 cm) incorporating the sampling devices. Here, TME ozonolysis was exclusively used for OH radical formation. Ozone was injected through a nozzle system into the gas mixture, containing TME, reduced-sulfur compounds and additives if needed, just before entering the middle section. The total flow was set at 30 litre min⁻¹ (STP) resulting in a residence time of 32 s in the reaction zone.

Humidified air in both setups was supplied by flushing a part of the air flow through three water saturators filled with water from an ultrapure water system (Barnstead, resistivity: 17.4 MΩ cm). The relative humidity of the reaction gas was continuously controlled at the outflow by a humidity sensor (Hygrosense HYTE). Ozone was monitored by a gas monitor (Thermo Scientific iQ 49) and the concentration of organic compounds by a proton transfer reaction - mass spectrometer (Ionicon, high sensitivity PTR-MS)⁵⁸. The “crude” air was taken from a pressure swing adsorption unit with further purification by means of absorber units filled with charcoal, a hopcalite (CuMnO_x) catalyst⁵⁹ and different activated 4 Å and 10 Å molecular sieves.

Reactant concentrations and conversion and the importance of OH + SO₂ and Criegee intermediate + SO₂

Initial reactant concentrations are either given in Supplementary Table 1 for the experiments described in the main text, Figs. 2–4, or in the figure captions. The amount of reacted CH₃SH in the IPN photolysis experiment (Fig. 2a) was measured in an additional run in the presence of SO₂ (for otherwise identical reaction conditions) by monitoring H₂SO₄ formation. The SO₂ concentration, 7.5 × 10¹¹ molecules cm⁻³, was chosen to such an extent that only 2% of formed OH radicals reacted with SO₂ and, thus, the product formation of the OH + CH₃SH reaction was not disturbed¹². Reacted CH₃SH is available from the measured H₂SO₄ (after correction of the fraction arising from CH₃SH oxidation) considering the OH reactivity in the parallel reactions OH + CH₃SH and OH + SO₂. In the case of TME ozonolysis for OH production, the amount of reacted CH₃SH or DMDS was calculated based on a detailed reaction scheme (Supplementary Table 4). Modelling calculations, including the IPN photolysis experiment, confirmed that H₂SO₄ production starting from the reaction of SO₂ with OH radicals or Criegee intermediates did not significantly influence the results of direct H₂SO₄ formation from the organic sulfur compounds.

Mass spectrometric analysis

Detection of H₂SO₄, CH₃SO₃H and other oxidation products was carried out using a Cl-API-TOF (chemical ionisation - atmospheric pressure interface - time-of-flight) mass spectrometer with a resolving power > 3000 Th/Th (Tofwerk) connected to a Boulder-type inlet system (Airmodus) operating with iodide (I⁻) and nitrate (NO₃⁻) as the reagent ions at atmospheric pressure^{12,31}.

In the case of ionisation by iodide, tert-butyl iodide premixed in a flask was added to a 35 litre min⁻¹ (STP) sheath flow of purified nitrogen leading to a tert-butyl iodide concentration of 4.8 × 10¹¹ molecules cm⁻³. Produced ions after ionisation with a ²⁴¹Am source were I⁻ and to a lesser amount I(H₂O)⁻. The ions from the sheath flow were guided into the sample flow by an electric field without mixing of both gas streams. In the case of ionisation by nitrate, an HNO₃ containing vial was connected to the 35 litre min⁻¹ (STP) flow without overflowing the HNO₃ sample. HNO₃ diffusion from the vial was found to be sufficient to form the reagent ions (HNO₃)_xNO₃⁻, x = 0, 1, 2, after ionisation.

Absolute signal calibration was used in the measurements of H₂SO₄ applying iodide and nitrate ionisation as well as in the

determination of SO₃, which was detected as the adduct (SO₃)NO₃⁻ and SO₄⁻^{60,61} using nitrate ionisation. H₂SO₄ and SO₃ production in the calibration experiments for wet (r.h. = 10%) and dry (r.h. <0.1%) conditions, respectively, was carried out via TME ozonolysis in the presence of SO₂⁶². The calibration factors obtained for H₂SO₄ were also taken for CH₃SO₃H. In the case of CH₃SO₂, CH₃SO₂OOH and CH₃SO₂OONO₂, a calculated calibration factor of 2 × 10⁹ molecules cm⁻³ was taken, resulting in lower limit concentrations for these products with an uncertainty of a factor of two^{31,45}.

Kinetic data analysis

H₂SO₄ and MSA wall loss in the LFT:

The rate law for H₂SO₄ is given by

$$\frac{d[H_2SO_4]}{dt} = P_{H_2SO_4} - k_{loss} \times [H_2SO_4] \quad (1)$$

assuming a time-independent production term of H₂SO₄, P_{H₂SO₄}. This assumption is justified because of constant OH radical production during the whole reaction time and practically constant reactant concentrations due to reactant conversions clearly smaller than 1% in each case. Integration of Eq. (1) with [H₂SO₄]_{t=0} = 0 yields:

$$[H_2SO_4]_t = \frac{P_{H_2SO_4}}{k_{loss}} (1 - \exp(-k_{loss} \times t)) \quad (2)$$

[H₂SO₄]_t = P_{H₂SO₄} × t follows for the wall-loss free H₂SO₄ concentration. Consequently, the relative H₂SO₄ loss in the tube is given by:

$$H_2SO_4 \text{ loss} = 1 - \frac{1}{k_{loss} \times t} (1 - \exp(-k_{loss} \times t)) \quad (3)$$

The value of k_{loss} can be described by the diffusion-controlled wall-loss term $\frac{3.65x \cdot D}{r^2}$ using an experimentally obtained H₂SO₄ diffusion coefficient D = 0.08 cm² s⁻¹⁶³ leading to k_{loss} = 0.018 s⁻¹. Based on that and for the reaction time of 32 s in the LFT, a H₂SO₄ loss of 24% was calculated using Eq. (3). Thus, the measured H₂SO₄ concentration was multiplied with 1.315 to consider the wall loss. The same was applied for MSA.

Determination of k₁₇ describing CH₃SO₃ → SO₃ + CH₃:

Assuming dominant loss of CH₃SO₃ via its decomposition into SO₃ and CH₃ and a time-independent production term of CH₃SO₃, P_{CH₃SO₃}, due to practically constant reactant conditions, the rate law of CH₃SO₃ is given by:

$$\frac{d[CH_3SO_3]}{dt} = P_{CH_3SO_3} - k_{17} \times [CH_3SO_3] \quad (4)$$

Integration of Eq. (4) with [CH₃SO₃]_{t=0} = 0 yields:

$$[CH_3SO_3]_t = \frac{P_{CH_3SO_3}}{k_{17}} (1 - \exp(-k_{17} \times t)) \quad (5)$$

The rate law of SO₃ formation is

$$\begin{aligned} \frac{d[SO_3]}{dt} &= k_{17} \times [CH_3SO_3] \\ &= P_{CH_3SO_3} \times (1 - \exp(-k_{17} \times t)) \end{aligned} \quad (6)$$

leading after integration with [SO₃]_{t=0} = 0 to:

$$\frac{[SO_3]_t}{P_{CH_3SO_3}} = t - \frac{1}{k_{17}} (1 - \exp(-k_{17} \times t)) \quad (7)$$

Because of immediate SO_3 conversion to H_2SO_4 under humid conditions, Eq. (7) can be written in the following way:

$$\frac{[\text{H}_2\text{SO}_4]_t}{P_{\text{CH}_3\text{SO}_3}} = t - \frac{1}{k_{17}} (1 - \exp(-k_{17} \times t)) \quad (8)$$

Equation (8) was used to determine k_{17} based on measured H_2SO_4 concentrations from $\text{OH} + \text{CH}_3\text{SH}$ depending on NO_2 additions in both flow systems, i.e. in the free-jet flow system with $t = 7.9$ s and in the LFT with $t = 32$ s for otherwise similar conditions (Supplementary Fig. 14 and Fig. 4d). The ratio $[\text{H}_2\text{SO}_4]_{32\text{s}}/[\text{H}_2\text{SO}_4]_{7.9\text{s}}$ was found to be 4.5 ± 0.6 with a corresponding ratio of the CH_3SO_3 production rates $P_{\text{CH}_3\text{SO}_3}$ of 1/2.27, that considered the different reactant concentrations in the experiments and the fraction of OH radicals reacting with CH_3SH . For the mean H_2SO_4 ratio of 4.5, $k_{17} = 0.076 \text{ s}^{-1}$ was calculated leading to $0.076^{+0.034}_{-0.025} \text{ s}^{-1}$ that involves the bounds of the H_2SO_4 ratio. Based on Eq. (9), which corresponds to Eq. (3) for H_2SO_4 loss,

$$\text{CH}_3\text{SO}_3 \text{ decomposition} = 1 - \frac{1}{k_{17} \times t} (1 - \exp(-k_{17} \times t)) \quad (9)$$

it was possible to calculate with $k_{17} = 0.076 \text{ s}^{-1}$, that 62% of formed CH_3SO_3 decomposed in the LFT ($t = 32$ s) making a correction factor of 1.6 necessary in order to account for total removal via pathway 17. It is to be noted, that the reaction of CH_3SH with CH_3SO_3 , pathway 19, does not influence this result as long as the contribution of this pathway (same CH_3SH concentration) is identical in both flow experiments.

Atmospheric modelling

Complex multiphase chemistry simulations were performed using the SPectral Aerosol Cloud Chemistry Interaction Model (SPACCIM)⁶⁴ to study the contributions of different reaction pathways from DMS, SO_2 and CH_3SH leading to sulfuric acid or its precursors under pristine marine conditions. It should be noted, that the applied model is not designed to simulate new particle formation. Thus, nucleation driven by gas-phase H_2SO_4 and resulting effects cannot be investigated. Therefore, we only focus on the chemical gas-phase H_2SO_4 formation in the present study.

In the model, the multiphase chemistry is described by combining the near-explicit gas-phase mechanism MCMv3.2^{65,66} and detailed aqueous-phase chemistry mechanism CAPRAM4.0 (Chemical Aqueous Phase RAdical Mechanism version 4.0)⁴⁷, respectively. This mechanism system describes the formation of gas-phase H_2SO_4 and aqueous sulfate in a very detailed manner. The representation of the specific multiphase chemistry of reactive halogen species and dimethyl sulfide, important for the marine atmosphere, is achieved through two additional reaction modules, CAPRAM-HM3.0⁴⁸ and CAPRAM-DML0²¹. With these two additional modules, CAPRAM4.0 includes almost all known sulfate formation pathways in the atmospheric aqueous phase, such as S(IV) oxidation by H_2O_2 , O_3 , HNO_4 , reactive halogen species (X_2^- radical or HOX, with $\text{X} = \text{Cl}, \text{Br}$ or I) or transition metal ions.

Due to the intended foci of the simulations, the complex multiphase DMS chemistry scheme of CAPRAM-DML0 has been upgraded with recent mechanism updates and an oxidation scheme for CH_3SH was implemented (Supplementary Table 5). The mechanistic updates comprise the formation of the hydroperoxymethyl thioformate (HPMTF) and its further oxidation in the gas phase. The gas-phase HPMTF oxidation follows mainly the proposed routes described by Wu et al. (2015)¹¹, considering SO_2 or OCS formation, only. Thus, HPMTF cannot contribute to the direct gas-phase formation of H_2SO_4 in this mechanism. Phase transfer and subsequent aqueous-phase processing of HPMTF, not included yet because of the current high uncertainties, do not change this. Briefly, the revised mechanism scheme contains 128 gas-phase reactions, 5 phase transfer processes and 50 aqueous-phase reactions.

In the process simulations, an aerosol particle spectrum representative for pristine marine conditions is included⁶⁷. The whole model setup (emission, deposition, initialisation of the gas-phase and particle-phase composition) is the same as applied in previous DMS chemistry studies^{21,48}. An exception is the newly included emission of CH_3SH (emission rate: $3.18 \times 10^3 \text{ molecules cm}^{-3} \text{ s}^{-1}$), which is a factor of ten lower compared to that of DMS. This difference is in line with field measurements, see attached Supplementary Dataset 1.

In total, six simulations were performed, separated into (i) three with (“Cloud”) and (ii) three without (“no Cloud”) cloud processing along the air parcel trajectory. The total simulation time is 108-hours but only day 2 to 4 were considered for data analysis to avoid spin-up effects. Runs are performed for summer conditions, with a boundary layer temperature and relative humidity of 280 K and 70% during non-cloud periods. In the simulations with cloud interactions, eight non-permanent clouds are considered. Every cloud exists for about two hours and occurs around noon and midnight, respectively. Cloud formation is achieved through adiabatic cooling of the air parcel 15 minutes before 11 a.m. and p.m., and the cloud evaporation is realised by adiabatic warming 15 minutes after 1 p.m. and a.m., respectively. Besides the two microphysical scenarios (“Cloud”, “no Cloud”), simulations were run with Henry’s Law constants implemented in the base mechanism²¹ and with lower Henry’s Law constants for DMSO ($H_{A,298\text{K}} = 2.43 \times 10^5 \text{ mol atm}^{-1}$), DMSO₂ ($H_{A,298\text{K}} = 1.18 \times 10^6 \text{ mol atm}^{-1}$), and MSIA ($H_{A,298\text{K}} = 1.69 \times 10^6 \text{ mol atm}^{-1}$) calculated by COSMOtherm²². The two uptake cases were performed to consider the potential uncertainty in the Henry’s Law constants and to study their impact of the sulfuric acid formation. In addition, simulations with an increased NO emission by a factor of ten were run using Henry’s Law constants implemented in the base mechanism. All simulation scenarios together with their individual configurations are outlined in Supplementary Table 2.

For the six different simulations, averaged net rates (in molecules $\text{cm}^{-3} \text{ s}^{-1}$) for the daytime oxidation of DMS, CH_3SH and SO_2 between the second to the fourth model day were calculated as well as primary daytime production rates of CH_3S and CH_3SO_2 . For the oxidation of DMS, we distinguish between rates of the addition and abstraction pathways. All calculated rates are given in Supplementary Table 3.

Data availability

The measurement data collected from the literature and used in this work are provided in the attached Supplementary Dataset 1. The data generated in this study are provided in the Supplementary Information. Source data are provided with this paper.

Code availability

The code of MCM is provided via <http://mcm.leeds.ac.uk/MCM> and CAPRAM code is available at <https://capram.tropos.de/>. The new and updated mechanism implementation data are provided in the Supplementary Information.

References

1. Charlson, R. J., Lovelock, J. E., Andreae, M. O. & Warren, S. G. Oceanic phytoplankton, atmospheric sulphur, cloud albedo and climate. *Nature* **326**, 655–661 (1987).
2. Bates, T. S., Charlson, R. J. & Gammon, R. H. Evidence for the climatic role of marine biogenic sulphur. *Nature* **329**, 319–321 (1987).
3. Twomey, S. The Influence of Pollution on the Shortwave Albedo of Clouds. *J. Atmos. Sci.* **34**, 1149–1152 (1977).
4. Albrecht, B. A. Aerosols, cloud microphysics, and fractional cloudiness. *Science* **245**, 1227–1230 (1989).
5. Lee, C.-L. & Brimblecombe, P. Anthropogenic contributions to global carbonyl sulfide, carbon disulfide and organosulfides fluxes. *Earth Sci. Rev.* **160**, 1–18 (2016).

6. Hynes, A. J., Wine, P. H. & Semmes, D. H. Kinetics and mechanism of hydroxyl reactions with organic sulfides. *J. Phys. Chem.* **90**, 4148–4156 (1986).
7. Tyndall, G. S. & Ravishankara, A. R. Kinetics and mechanisms of the reactions of methylthiyl with oxygen and nitrogen dioxide at 298 K. *J. Phys. Chem.* **93**, 2426–2435 (1989).
8. Turnipseed, A. A., Barone, S. B. & Ravishankara, A. R. Observation of methylthiyl radical addition to oxygen in the gas phase. *J. Phys. Chem.* **96**, 7502–7505 (1992).
9. Barnes, I., Hjorth, J. & Mihalopoulos, N. Dimethyl sulfide and dimethyl sulfoxide and their oxidation in the atmosphere. *Chem. Rev.* **106**, 940–975 (2006).
10. Turnipseed, A. A., Barone, S. B. & Ravishankara, A. R. Reactions of methylthio and (methylthio)dioxy with ozone, nitrogen dioxide, and nitric oxide. *J. Phys. Chem.* **97**, 5926–5934 (1993).
11. Wu, R., Wang, S. & Wang, L. New mechanism for the atmospheric oxidation of dimethyl sulfide. The importance of intramolecular hydrogen shift in a $\text{CH}_3\text{SCH}_2\text{OO}$ radical. *J. Phys. Chem. A* **119**, 112–117 (2015).
12. Berndt, T. et al. Fast Peroxy Radical Isomerization and OH Recycling in the Reaction of OH Radicals with Dimethyl Sulfide. *J. Phys. Chem. Lett.* **10**, 6478–6483 (2019).
13. Veres, P. R. et al. Global airborne sampling reveals a previously unobserved dimethyl sulfide oxidation mechanism in the marine atmosphere. *P. Natl Acad. Sci. USA* **117**, 4505–4510 (2020).
14. Ye, Q. et al. Organic Sulfur Products and Peroxy Radical Isomerization in the OH Oxidation of Dimethyl Sulfide. *ACS Earth Space Chem.* **5**, 2013–2020 (2021).
15. Wu, Z. et al. Spectroscopic characterization of two peroxy radicals during the O_2 -oxidation of the methylthio radical. *Commun. Chem.* **5**, 19 (2022).
16. Jernigan, C. M. et al. Efficient Production of Carbonyl Sulfide in the Low- NO_x Oxidation of Dimethyl Sulfide. *Geophys. Res. Lett.* **49**, 1–11 (2022).
17. Shen, J. et al. High Gas-Phase Methanesulfonic Acid Production in the OH-Initiated Oxidation of Dimethyl Sulfide at Low Temperatures. *Environ. Sci. Technol.* **56**, 13931–13944 (2022).
18. Arsene, C., Barnes, I. & Becker, K. H. FT-IR product study of the photo-oxidation of dimethyl sulfide: Temperature and O_2 partial pressure dependence. *Phys. Chem. Chem. Phys.* **1**, 5463–5470 (1999).
19. Yin, F., Grosjean, D. & Seinfeld, J. H. Photooxidation of dimethyl sulfide and dimethyl disulfide. I: Mechanism development. *J. Atmos. Chem.* **11**, 309–364 (1990).
20. Campolongo, F., Saltelli, A., Jensen, N. R., Wilson, J. & Hjorth, J. The Role of Multiphase Chemistry in the Oxidation of Dimethylsulphide (DMS). A Latitude Dependent Analysis. *J. Atmos. Chem.* **32**, 327–356 (1999).
21. Hoffmann, E. H. et al. An advanced modeling study on the impacts and atmospheric implications of multiphase dimethyl sulfide chemistry. *P. Natl Acad. Sci. USA* **113**, 11776–11781 (2016).
22. Wollesen de Jonge, R. et al. Secondary aerosol formation from dimethyl sulfide – improved mechanistic understanding based on smog chamber experiments and modelling. *Atmos. Chem. Phys.* **21**, 9955–9976 (2021).
23. Cox, R. A. Photochemical oxidation of atmospheric sulphur dioxide. *Philos. Trans. R. Soc. A* **290**, 543–550 (1979).
24. Davis, D. D., Ravishankara, A. R. & Fischer, S. SO_2 oxidation via the hydroxyl radical: Atmospheric fate of HSO_x radicals. *Geophys. Res. Lett.* **6**, 113–116 (1979).
25. Cox, R. A. & Penkett, S. A. Photo-oxidation of atmospheric SO_2 . *Nature* **229**, 486–488 (1971).
26. Mauldin, R. L. 3rd. et al. A new atmospherically relevant oxidant of sulphur dioxide. *Nature* **488**, 193–196 (2012).
27. Bandy, A. R., Scott, D. L., Blomquist, B. W., Chen, S. M. & Thornton, D. C. Low yields of SO_2 from dimethyl sulfide oxidation in the marine boundary layer. *Geophys. Res. Lett.* **19**, 1125–1127 (1992).
28. Lin, X. & Chameides, W. L. CCN formation from DMS oxidation without SO_2 acting as an intermediate. *Geophys. Res. Lett.* **20**, 579–582 (1993).
29. Berndt, T., Herrmann, H., Sipila, M. & Kulmala, M. Highly Oxidized Second-Generation Products from the Gas-Phase Reaction of OH Radicals with Isoprene. *J. Phys. Chem. A* **120**, 10150–10159 (2016).
30. Berndt, T. et al. Hydroxyl radical-induced formation of highly oxidized organic compounds. *Nat. Commun.* **7**, 13677 (2016).
31. Berndt, T., Hyttinen, N., Herrmann, H. & Hansel, A. First oxidation products from the reaction of hydroxyl radicals with isoprene for pristine environmental conditions. *Commun. Chem.* **2**, 21 (2019).
32. Berndt, T. et al. SO_2 formation and peroxy radical isomerization in the atmospheric reaction of OH radicals with dimethyl disulfide. *Chem. Commun.* **56**, 13634–13637 (2020).
33. Chen, J., Berndt, T., Moller, K. H., Lane, J. R. & Kjaergaard, H. G. Atmospheric Fate of the CH_3SOO Radical from the $\text{CH}_3\text{S} + \text{O}_2$ Equilibrium. *J. Phys. Chem. A* **125**, 8933–8941 (2021).
34. Tyndall, G. S. & Ravishankara, A. R. Kinetics of the reaction of the methylthio radical with ozone at 298 K. *J. Phys. Chem.* **93**, 4707–4710 (1989).
35. Salta, Z., Kosmas, A. M. & Lesar, A. Computational investigation of the peroxy radicals $\text{CH}_3\text{S}(\text{O})_n\text{OO}$ and the peroxy nitrates $\text{CH}_3\text{S}(\text{O})_n\text{OONO}_2$ ($n = 0, 1, 2$). *Comput. Theor. Chem.* **1001**, 67–76 (2012).
36. Domine, F., Ravishankara, A. R. & Howard, C. J. Kinetics and mechanisms of the reactions of methylthio, methylsulfinyl, and methylthio radicals with ozone at 300 K and low pressures. *J. Phys. Chem.* **96**, 2171–2178 (2002).
37. Ray, A., Vassalli, I., Laverdet, G. & Le Bras, G. Kinetics of the Thermal Decomposition of the CH_3SO_2 Radical and Its Reaction with NO_2 at 1 Torr and 298 K. *J. Phys. Chem.* **100**, 8895–8900 (1996).
38. Mardyukov, A. & Schreiner, P. R. Atmospherically Relevant Radicals Derived from the Oxidation of Dimethyl Sulfide. *Acc. Chem. Res.* **51**, 475–483 (2018).
39. Tyndall, G. S. & Ravishankara, A. R. Atmospheric oxidation of reduced sulfur species. *Int. J. Chem. Kinet.* **23**, 483–527 (1991).
40. Wine, P. H., Kreutter, N. M., Gump, C. A. & Ravishankara, A. R. Kinetics of hydroxyl radical reactions with the atmospheric sulfur compounds hydrogen sulfide, methanethiol, ethanethiol, and dimethyl disulfide. *J. Phys. Chem.* **85**, 2660–2665 (1981).
41. Domine, F., Murrells, T. P. & Howard, C. J. Kinetics of the reactions of nitrogen dioxide with CH_3S , CH_3SO , CH_3SS , and CH_3SSO at 297 K and 1 torr. *J. Phys. Chem.* **94**, 5839–5847 (2002).
42. Saltelli, A. & Hjorth, J. Uncertainty and sensitivity analyses of OH-initiated dimethyl sulphide (DMS) oxidation kinetics. *J. Atmos. Chem.* **21**, 187–221 (1995).
43. Cooper, O. R. et al. Global distribution and trends of tropospheric ozone: An observation-based review. *Elem. Sci. Anth.* **2**, 1–28 (2014).
44. Kroll, J. H., Sahay, S. R., Anderson, J. G., Demerjian, K. L. & Donahue, N. M. Mechanism of HO_x Formation in the Gas-Phase Ozone-Alkene Reaction. 2. Prompt versus Thermal Dissociation of Carbonyl Oxides to Form OH. *J. Phys. Chem. A* **105**, 4446–4457 (2001).
45. Berndt, T. et al. Accretion Product Formation from Self- and Cross-Reactions of RO_2 Radicals in the Atmosphere. *Angew. Chem. Int. Ed. Engl.* **57**, 3820–3824 (2018).
46. Orlando, J. J. & Tyndall, G. S. Laboratory studies of organic peroxy radical chemistry: an overview with emphasis on recent issues of atmospheric significance. *Chem. Soc. Rev.* **41**, 6294–6317 (2012).
47. Bräuer, P. et al. Development of a protocol for the auto-generation of explicit aqueous-phase oxidation schemes of organic compounds. *Atmos. Chem. Phys.* **19**, 9209–9239 (2019).

48. Hoffmann, E. H., Tilgner, A., Vogelsberg, U., Wolke, R. & Herrmann, H. Near-Explicit Multiphase Modeling of Halogen Chemistry in a Mixed Urban and Maritime Coastal Area. *ACS Earth Space Chem.* **3**, 2452–2471 (2019).
49. Kukui, A., Borissenko, D., Laverdet, G. & Le Bras, G. Gas-Phase Reactions of OH Radicals with Dimethyl Sulfoxide and Methane Sulfinic Acid Using Turbulent Flow Reactor and Chemical Ionization Mass Spectrometry. *J. Phys. Chem. A* **107**, 5732–5742 (2003).
50. de Bruyn, W. J., Harvey, M., Caine, J. M. & Saltzman, E. S. DMS and SO₂ at Baring Head, New Zealand: Implications for the Yield of SO₂ from DMS. *J. Atmos. Chem.* **41**, 189–209 (2002).
51. Wehner, B. et al. Observations of new particle formation in enhanced UV irradiance zones near cumulus clouds. *Atmos. Chem. Phys.* **15**, 11701–11711 (2015).
52. Kerminen, V.-M. et al. Atmospheric new particle formation and growth: review of field observations. *Environ. Res. Lett.* **13**, 1–38 (2018).
53. Mauldin, R. L. et al. New insights on OH: Measurements around and in clouds. *Geophys. Res. Lett.* **24**, 3033–3036 (1997).
54. Scholz, W. et al. Measurement report: Long-range transport and the fate of dimethyl sulfide oxidation products in the free troposphere derived from observations at the high-altitude research station Chacaltaya (5240 m a.s.l.) in the Bolivian Andes. *Atmos. Chem. Phys.* **23**, 895–920 (2023).
55. McCoy, I. L. et al. Influences of Recent Particle Formation on Southern Ocean Aerosol Variability and Low Cloud Properties. *J. Geophys. Res. -Atmos.* **126**, 1–27 (2021).
56. Berndt, T. et al. Kinetics of the unimolecular reaction of CH₂OO and the bimolecular reactions with the water monomer, acetaldehyde and acetone under atmospheric conditions. *Phys. Chem. Chem. Phys.* **17**, 19862–19873 (2015).
57. Raff, J. D. & Finlayson-Pitts, B. J. Hydroxyl radical quantum yields from isopropyl nitrite photolysis in air. *Environ. Sci. Technol.* **44**, 8150–8155 (2010).
58. Lindinger, W. & Jordan, A. Proton-transfer-reaction mass spectrometry (PTR-MS): on-line monitoring of volatile organic compounds at pptv levels. *Chem. Soc. Rev.* **27**, 347–375 (1998).
59. Dey, S., Dhal, G. C., Mohan, D. & Prasad, R. Ambient temperature complete oxidation of carbon monoxide using hopcalite catalysts for fire escape mask applications. *Adv. Compos. Hybrid. Mater.* **2**, 501–519 (2019).
60. Arnold, S. T., Morris, R. A., Viggiano, A. A. & Jayne, J. T. Ion chemistry relevant for chemical ionization detection of SO₃. *J. Geophys. Res. -Atmos.* **100**, 14141–14146 (1995).
61. Yao, L. et al. Unprecedented Ambient Sulfur Trioxide (SO₃) Detection: Possible Formation Mechanism and Atmospheric Implications. *Environ. Sci. Technol. Lett.* **7**, 809–818 (2020).
62. Berndt, T. Peroxy Radical Processes and Product Formation in the OH Radical-Initiated Oxidation of alpha-Pinene for Near-Atmospheric Conditions. *J. Phys. Chem. A* **125**, 9151–9160 (2021).
63. Hanson, D. R. & Eisele, F. Diffusion of H₂SO₄ in Humidified Nitrogen: Hydrated H₂SO₄. *J. Phys. Chem. A* **104**, 1715–1719 (2000).
64. Wolke, R. et al. SPACCIM: A parcel model with detailed microphysics and complex multiphase chemistry. *Atmos. Environ.* **39**, 4375–4388 (2005).
65. Jenkin, M. E., Saunders, S. M. & Pilling, M. J. The tropospheric degradation of volatile organic compounds: a protocol for mechanism development. *Atmos. Environ.* **31**, 81–104 (1997).
66. Saunders, S. M., Jenkin, M. E., Derwent, R. G. & Pilling, M. J. *Atmos. Chem. Phys.* **3**, 161–180, <https://doi.org/10.5194/acp-3-161-2003> (2003), via website: <http://mcm.leeds.ac.uk/MCM>.
67. Poppe, D. et al. Scenarios for Modeling Multiphase Tropospheric Chemistry. *J. Atmos. Chem.* **40**, 77–86 (2001).
68. R Core Team. R: A language and environment for statistical computing. R Foundation for Statistical Computing, Vienna, Austria. <https://www.R-project.org/>. (2017).

Acknowledgements

The authors thanks K. Pielok, R. Gräfe and A. Rohmer for technical assistance and the tofTools team for providing the data analysis tools. T.B. thanks J. Chen and H.G. Kjaergaard, University of Copenhagen, for motivating discussions. Support came from the Deutsche Forschungsgemeinschaft, project ADOniS (grant HE 3086/53-1, T.B., E.H.H., A.T. and H.H.).

Author contributions

T.B. designed and carried out the experiments and did the data analysis. F.S. and T.B. constructed the flow systems. E.H.H., A.T. and H.H. conducted the modelling work. T.B., E.H.H. and A.T. wrote the draft and all authors contributed to the final version of the manuscript.

Funding

Open Access funding enabled and organized by Projekt DEAL.

Competing interests

The authors declare no competing interests.

Additional information

Supplementary information The online version contains supplementary material available at <https://doi.org/10.1038/s41467-023-40586-2>.

Correspondence and requests for materials should be addressed to Torsten Berndt.

Peer review information *Nature Communications* thanks the anonymous reviewers for their contribution to the peer review of this work. A peer review file is available.

Reprints and permissions information is available at <http://www.nature.com/reprints>

Publisher's note Springer Nature remains neutral with regard to jurisdictional claims in published maps and institutional affiliations.

Open Access This article is licensed under a Creative Commons Attribution 4.0 International License, which permits use, sharing, adaptation, distribution and reproduction in any medium or format, as long as you give appropriate credit to the original author(s) and the source, provide a link to the Creative Commons license, and indicate if changes were made. The images or other third party material in this article are included in the article's Creative Commons license, unless indicated otherwise in a credit line to the material. If material is not included in the article's Creative Commons license and your intended use is not permitted by statutory regulation or exceeds the permitted use, you will need to obtain permission directly from the copyright holder. To view a copy of this license, visit <http://creativecommons.org/licenses/by/4.0/>.

© The Author(s) 2023